Electronic Supplementary Material (ESI) for Nanoscale.

Terphenylthiazole-based self-assembled monolayers on cobalt with high conductance photo-switching ratio for spintronics

Vladimir Prudkovskiy,[a] Imane Arbouch,[b] Anne Léaustic,[c] Pei Yu,[c,]*

Colin Van Dyck,[b] David Guérin,[a] Stéphane Lenfant,[a]

Talal Mallah,[c] Jérôme Cornil,[b,] and Dominique Vuillaume.[a,*]*

a) Institute for Electronics Microelectronics and Nanotechnology (IEMN), CNRS, Av. Poincaré, Villeneuve d'Ascq, France.

b) Laboratory for Chemistry of Novel Materials, University of Mons, Place du parc 20, 7000 Mons, Belgium.

c) Institut de Chimie Moléculaire et des Matériaux d'Orsay (ICMMO), CNRS, Université Paris-Saclay, 91405 Orsay Cedex, France

pei.yu@universite-paris-saclay.fr
jerome.cornil@umons.ac.be
dominique.vuillaume@iemn.fr

SUPPORTING INFORMATION

Section 1. Synthesis and NMR characterization.

Air-sensitive syntheses were performed under argon using standard Schlenk techniques. Chemicals and solvents were used as received unless otherwise stated. Anhydrous solvents, when necessary, were dried using standard methods. Thin layer chromatography (TLC) was performed on silica gel 60 F_{254} while column chromatography was carried out on silica gel (0.063-0.2 mm). The two new

photochromic terphenylthiazoles A and B were prepared according to the synthetic routes shown in Scheme 1.

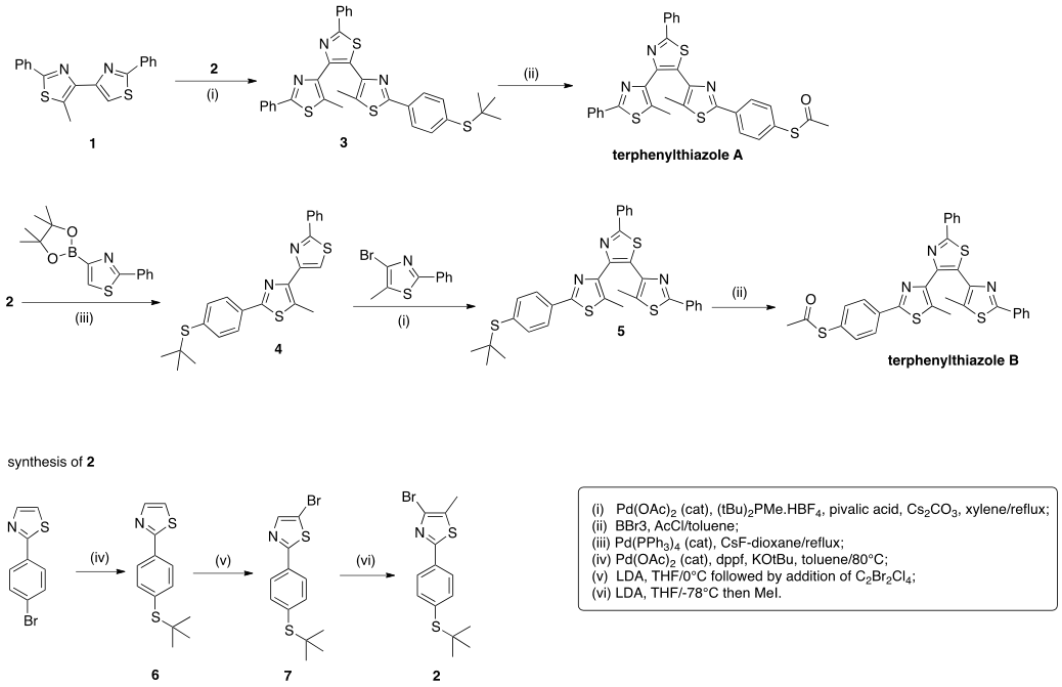

Scheme S1

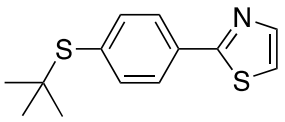

6

2-(4-Br-phenyl)-thiazole[1] (2.40 g, 10 mmol), KOtBu (1.57 g, 14 mmol), Pd(OAc)2 (23 mg, 0.10 mmol), dppf (60 mg, 0.11 mmol) in a Schlenk were purged before dry toluene (20 ml) and then 2-Methyl-2-propanethiol (1,4 ml, 12.4 mmol) were introduced. The mixture was heated at 80°C under Argon and monitored by TLC until all 2-(4-Br-phenyl)-thiazole was consumed (ca 3 hours). Once cooled to RT water (20 ml) and EtOAc (30 ml) were added to the mixture and the aqueous phase was extracted with EtOAc (2x20 ml). Combined organic phase was washed with water (50 ml) and dried over Na_2SO_4. Vacuum evaporation of the solvents gave a light brown crystalline solid (2.375 g, 95%), which is pure enough for the

next step or could be further purified by column chromatography (silica gel, dichloromethane) to yield a colorless crystalline solid (2.255 g, yield 90%).

^{1}HNMR ($CDCl_3$): 7.95 (d, J = 8.3 Hz, 2H), 7.90 (d, J = 3.5 Hz, 1H), 7.66 (d, J = 8.3 Hz, 2H), 7.37 (d, J = 3.5 Hz, 1H), 1.32 (s, 9H). HRMS (ESI): calculated for $C_{13}H_{15}NS_2$ $[M+H]^+$: 250.0719, found: 250.0713.

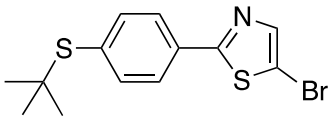

7

Thiazole 6 (673 mg, 2.7 mmol) was purged before dry THF (20 ml) was introduced and the solution cooled down to 0°C. LDA (2M, 2.0 ml) was added and the resulting deep violet solution was kept at the same temperature for ca 20 min. before 1,2-dibromotetrachloroethane (980 mg, 3 mmol) was added once as solid. The solution turned immediately brown and the solution was warmed to RT and left overnight. Aqueous NH_4Cl solution (1M, 20 ml) and then diethyl ether (20 ml) were added and stirred a few minutes before the organic phase was collected. The aqueous phase was extracted with diethyl ether (20 ml) and combined organic phase was washed with water (40 ml) and dried over Na_2SO_4. After evaporation of the solvents, the solid residue was submitted to column chromatography (silica gel, dichloromethane) to yield thiazole 7 as a light yellow, crystalline solid (755 mg, yield 85%).

^{1}HNMR ($CDCl_3$): 7.82 (d, J = 8 Hz, 2H), 7.75 (s, 1H), 7.59 (d, J = 8 Hz, 2H), 1.32 (s, 9H). HRMS (ESI): calculated for $C_{13}H_{15}BrNS_2$ $[M+H]^+$: 327.9824, found: 327.9820.

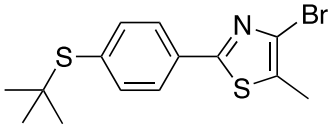

2

Thiazole 2 is readily accessed through Halogen-Dance reaction.[2, 3] Thiazole 7 (1.315 g, 4 mmol) was purged and dry THF (25 ml) was introduced under argon. The resulting solution was cooled to -78°C before LDA (2M, 3 ml) was added dropwise to give a deep violet solution. After 20 min at the same temperature, iodomethane (0.38 ml, 6 mmol) was added and the solution was slowly warmed to RT and left overnight. To the resulting solution, aqueous NH_4Cl solution (1M, 20 ml) and then diethyl ether (30 ml) were added and stirred a few min. before the organic phase was collected. The aqueous phase was extracted with diethyl ether (20 ml) and combined organic phase was washed with water (40 ml) and dried over Na_2SO_4. After evaporation of solvents, the residue was purified by column chromatography (silica gel, dichloromethane) to give thiazole 2 as an off-white crystalline solid (1.250 g, yield 91%).

^{1}HNMR ($CDCl_3$): 7.83 (d, J = 8.2 Hz, 2H), 7.57 (d, 2H), 2.45 (s, 3H), 1.31 (s, 9H). HRMS (ESI): calculated for $C_{14}H_{17}BrNS_2$ $[M+H]^+$: 341.9980, found: 341.9969.

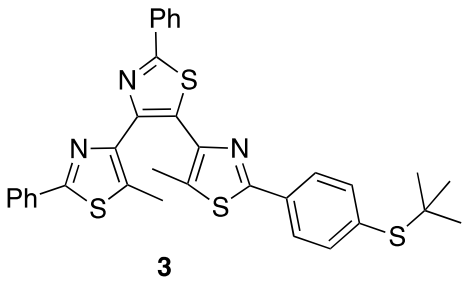

3

The title compound was prepared using a reported method via a palladium-catalyzed cross-coupling reaction through a direct C-H activation of thiazole.[4] Bisthiazole 1 [5] (290 mg, 0.87 mmol), thiazole 2 (304 mg, 0.88 mmol), pivalic acid (34 mg, 0.33 mmol), $P(tBu)_2Me.HBF_4$, 30 mg, 0.12 mmol), $Pd(OAc)_2$ (23 mg, 0.1 mmol) and Cs_2CO_3 (567 mg, 1.74 mmol) were purged before xylene (5 ml) was introduced under argon. The mixture was refluxed overnight under argon, and dichloromethane (20 ml) then water (20 ml) were added into the mixture at RT. The aqueous phase was extracted with dichloromethane (4x20 ml) and combined organic phase was washed with water (40 ml) and dried over Na_2SO_4. After

evaporation of the solvents, the residue was purified by column chromatography (silica gel, dichloromethane). The photochromic fraction was evaporated under reduced pressure and the residue was taken in methanol (10 ml) and triturated. The resulting solid was filtered and washed with methanol and dried under vacuum to give terphenylthiazole 3 a light yellow solid (448 mg, yield 86%).

^{1}HNMR ($CDCl_3$): 8.05-8.08 (m, 2H), 7.89 (d, J = 8.6 Hz, 2H), 7.77-7.80 (m, 2H), 7.58 (d, J = 8.6 Hz, 2H), 7.46-7.48 (m, 3H), 7.33-7.35 (m, 3H), 2.55 (s, 3H), 2.13 (s, 3H), 1.32 (s, 9H). HRMS (ESI): calculated for $C_{33}H_{30}N_3S_4$ $[M+H]^+$: 596.1317, found: 596.1300.

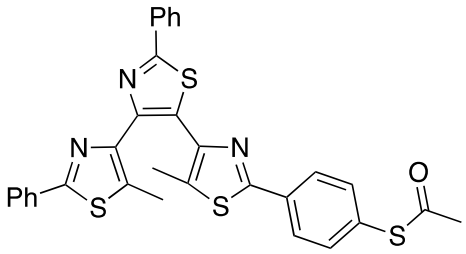

terphenylthiazole A

The deprotection of terbutyl thiol and its protection by acetyl group was carried out using BBr_3 and AcCl according to known literature method.[6] Terphenylthiazole 3 (300 mg, 0.5 mmol) was purged before addition of dry toluene (5 ml) followed by acetyl chloride (300 µl, 4.2 mmol). BBr_3 solution (1M in dichloromethane, 2.6 ml) was added under Argon at 0°C and the mixture stirred at that temperature then at RT overnight. Water (10 ml) was slowly added to destroy the excess of BBr_3 and mixture was then extracted with dichloromethane (2x20 ml). Combined organic phase was washed with brine (30 ml) and dried over Na_2SO_4. After evaporation of the solvent, the residue was purified by column chromatography (silica gel, DCM to 2-3% Et_2O) and the fraction containing terphenylthiazole 3 was evaporated under reduced pressure to give a gum-like solid, which was taken up with MeOH (10 ml) and stirred at RT to give the title compound as an off-white solid (188 mg, yield 65%).

^{1}HNMR ($CDCl_3$): 8.05-8.08 (m, 2H), 7.97 (d, J = 8.6 Hz, 2H), 7.77-7.80 (m, 2H), 7.46-7.49 (m, 5H), 7.34-7.36 (m, 3H), 2.55 (s, 3H), 2.45 (s, 3H), 2.12 (s, 3H).

^{13}CNMR ($CDCl_3$): 193.63, 167.30, 164.01, 163.01, 147.70, 146.19, 144.04, 134.76, 134.31, 133.57, 133.55, 133.09, 130.24, 129.69, 129.61, 128.93, 128.78, 126.94, 126.65, 126.29, 30.38, 12.75, 12.41.

HRMS (ESI): calculated for $C_{31}H_{24}N_3OS_4$ $[M+H]^+$: 582.0797, found: 582.0777.

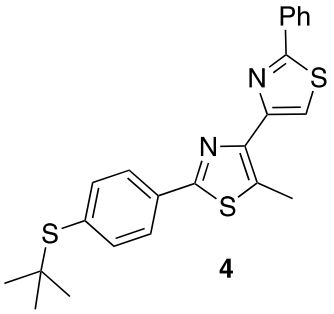

4

Thiazole 4 was prepared by Suzuki cross-coupling between thiazole 2 and 2-phenyl-4-(4,4,5,5-tetramethyl[1,3,2]dioxaborolan-2-yl)-thiazole[7] (2-Ph-4-Bpin-thiazole). Thiazole 2 (512 mg, 1.5 mmol), 2-Ph-4-Bpin-thiazole (525 mg, 1.83 mmol), $Pd(PPh_3)_4$ (72 mg, 0.062 mmol) and CsF (570 mg, 3.75 mmol) were purged before anhydrous dioxane (30 ml) was introduced under argon. The mixture was heated and refluxed under Argon for ca 6 hours and cooled to RT. Water (30 ml) and chloroform (30 ml) were added and organic phase collected. The aqueous phase was extracted with chloroform (25 ml), and combined organic phase was washed with water (50 ml) and dried over Na_2SO_4. Evaporation of the solvents led to a brown oil, to which MeOH (10 ml) was added and stirred at RT until a crystalline solid was formed. After filtration and washing with MeOH bisthiazole 4 was obtained as a slightly blueish solid (due to the presence of a very few closed form) (550 mg, 87% yield), which was pure enough for the next step.

^{1}HNMR ($CDCl_3$): 8.11 (s, 1H), 8.02-8.05 (m, 2H), 7.99 (d, J = 8.6 Hz, 2H), 7.63 (d, J = 8.1 Hz, 2H), 7.46-7.48 (m, 3H), 3.00 (s, 3H), 1.33 (s, 9H). HRMS (ESI): calculated for $C_{23}H_{23}N_2S_3$ $[M+H]^+$: 423.1018, found: 423.0997.

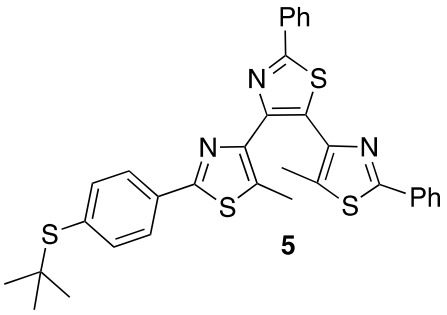

5

Thiazole 5 was synthesized in a similar way as terphenylthiazole 3. 2-Phenyl-4-Bpin-5-Methyl-thiazole[8] (280 mg, 1.1 mmol), thiazole 4 (405 mg, 1.1 mmol), pivalic acid (43 mg, 0.38 mmol), $P(tBu)_2Me.HBF_4$, (38 mg, 0.15 mmol), $Pd(OAc)_2$ (30 mg, 0.13 mmol) and Cs_2CO_3 (720 mg, 2.2 mmol) were purged before xylene (7 ml) was introduced under argon. The mixture was refluxed overnight under argon, and dichloromethane (30 ml) then water (30 ml) were added into the mixture at RT. The aqueous phase was extracted with dichloromethane (2x25 ml) and combined organic phase was washed with water (40 ml) and dried over Na_2SO_4. After evaporation of the solvents and the solid residue was stirred with MeOH (15 ml) overnight to give thiazole 5 as an off-white solid, which was used for the next step without further purification (600 mg, 91% yield).

^{1}HNMR ($CDCl_3$): 8.06-8.08 (m, 2H), 7.95-7.97 (m, 2H), 7.73 (d, J = 8 Hz, 2H), 7.42-7.49 (m, 8H), 2.59 (s, 3H), 2.18 (s, 3H), 1.29 (s, 9H). HRMS (ESI): calculated for $C_{33}H_{30}N_3S_4$ $[M+H]^+$: 596.1317, found: 596.1293.

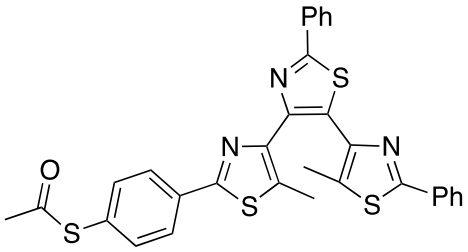

terphenylthiazole B

Terphenylthiazole 5 (302 mg, 0.5 mmol) was purged before addition of dry toluene (5 ml) followed by acetyl chloride (300 µl, 4.2 mmol). BBr_3 solution (1M in dichloromethane, 2.6 ml) was added under Argon at 0°C and the mixture was then stirred at RT overnight. Water (10 ml) was slowly added to destroy the excess of BBr_3 and mixture was then extracted with dichloromethane (2X20 ml). Combined organic phase was washed with brine (30 ml) and dried over Na_2SO_4. After evaporation of the solvent, the residue was purified by column chromatography (silica gel, DCM to 2-3% Et_2O) and the fraction containing terphenylthiazole 3 was evaporated under reduced pressure to give a greenish oil, which was taken up with MeOH (10 ml) and stirred at RT to give the title compound as light cream solid (206 mg, yield 70%).

^{1}HNMR ($CDCl_3$): 8.05-8.08 (m, 2H), 7.92-7.95 (m, 2H), 7.82 (d, J = 8 Hz, 2H), 7.37-7.48 (m, 8H), 2.57 (s, 3H), 2.43 (s, 3H), 2.11 (s, 3H).

^{13}CNMR ($CDCl_3$): 193.57, 167.05, 164.13, 162.34, 147.48, 146.45, 143.63, 134.66, 134.53, 133.83, 133.54, 133.41, 132.39, 130.23, 129.98, 129.25, 128.91, 126.89, 126.59, 30.31, 12.80, 12.35.

HRMS (ESI): calculated for $C_{31}H_{24}N_3OS_4$ $[M+H]^+$: 582.0797, found: 582.0770.

Section 2. Electrodes and SAMs fabrication.

General conditions of the process.

To prevent oxidation of the cobalt substrates, all the preparation of samples (i.e. from metal deposition to grafting of SAMs) was carried out in a nitrogen

MBRAUN glovebox (H_2O and O_2 levels below 5 ppm). The glassware was oven dried at 120°C overnight before insertion inside the glovebox to remove residual adsorbed water. The solvents used for the preparation of SAMs (absolute ethanol, tetrahydrofuran) were all purchased anhydrous from Sigma Aldrich. They were stored for 5 days over freshly activated 4 Å molecular sieves (activation for 18h at 150°C under vacuum), then they were degassed with nitrogen for at least 15 min.

Bottom metal electrode fabrication.

Ultraflat template-stripped gold surfaces (^{TS}Au), with rms roughness of ~0.4 nm were prepared according to the method developed by the Whitesides group.[9, 10] In brief, a 300−500 nm thick Au film was evaporated on a very flat silicon wafer covered by its native SiO_2 (rms roughness of ~0.4 nm), which was previously carefully cleaned by piranha solution (30 min in 7:3 H_2SO_4/H_2O_2 (v/v); ***Caution***: Piranha solution is a strong oxidizer and reacts exothermically with organics), rinsed with deionized (DI) water, and dried under a stream of nitrogen. Clean 10x10 mm pieces of glass slide (ultrasonicated in acetone for 5 min, ultrasonicated in 2-propanol for 5 min, and UV irradiated in ozone for 10 min) were glued on the evaporated Au film (UV-polymerizable glue, NOA61 from Epotecny), then mechanically peeled off providing the ^{TS}Au film attached on the glass side (Au film is cut with a razor blade around the glass piece).

Cobalt substrates were prepared by evaporating about 40 nm of cobalt on cleaved (12×10 mm) highly phosphorus-doped n-Si(100) substrates, resistivity < 5.10^{-3} Ω.cm (from Siltronix), covered by native oxide, cleaned by 5 min sonication in acetone and isopropanol, then rinsed with isopropanol and dried under N_2 flow. The evaporation of 99.99% purity cobalt pellets (Neyco) was realized by Joule effect in a vacuum evaporation system (Edwards Auto306) placed inside the glovebox. The cobalt deposition was realized under a 10^{-6} mbar vacuum and at a low rate deposition between 2 and 5 Å/s in order to minimize roughness.

***Self-assembled monolayers of TPT*.**

SAMs of the open forms of TPT(A) and TPT(B) on gold and cobalt were prepared from the acetyl-protected thiols by spontaneous assembly at metal surfaces via Au-S or Co-S bonds (see XPS section), without deprotection. Indeed thioacetates are known to undergo spontaneous deprotection at various metal surfaces like gold or silver.[11, 12] The freshly peeled off ^{TS}Au samples were immediately immersed in millimolar solutions of TPT in anhydrous ethanol/THF (80:20 v/v) for 3 days in the dark. This solvent mixture was compatible with the ^{TS}Au glue. Then samples were rinsed with degassed anhydrous THF and dried under N_2 stream. In a glovebox, the freshly evaporated Co substrates were immediately immersed in millimolar solutions of TPT in anhydrous ethanol/THF (80:20 v/v) for 1 day in the dark. Then samples were rinsed with degassed anhydrous ethanol, dried under N_2 stream and stored in the glovebox.

Section 3. UV-vis spectroscopy.

The reversible isomerization “open to close” of TPT molecules was checked by UV-vis spectroscopy in solution (~µM in CH_2Cl_2). UV-Vis absorption spectra were recorded on a Lambda 800 Perkin-Elmer spectrometer. For the UV irradiation of the solutions, we used a 365 nm chromatography lamp (Vilbert Lourmat, light intensity : 2 mW/cm^2 at 1 cm distance). For visible irradiation we used a halogen lamp (LEICA model CLS 150X) centered at 600 nm (light intensity : 220 mW/cm^2 at 1 cm distance). This experiment performed on µM solutions of TPT(A) and TPT(B) in DCM shows (Fig. S1) that, as expected, irradiation at 365 nm produces a strong absorption peak centered at 600-630nm corresponding to the formation of the closed form with the π-conjugation extended throughout the molecule. The photostationary state is reached after ~10 min of UV irradiation. Then irradiation at 650 nm causes disappearance of the 600-630 nm band and return to the open form. Return to the initial conditions is achieved by a short

irradiation in visible light (10-20s). The reversibility, tested for TPT(A), is particularly good after several irradiation cycles (inset Fig. S1).

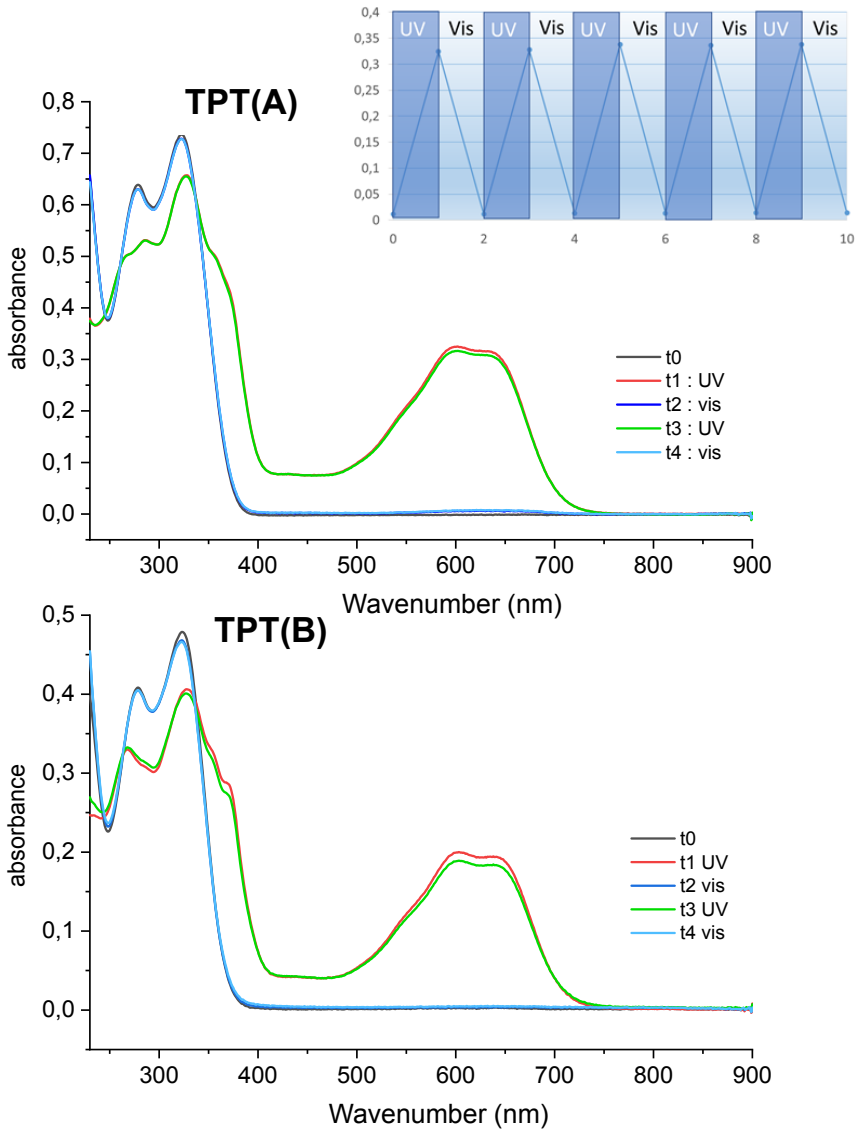

Figure S1. *UV-vis absorbance spectra of TPT(A) (top) and TPT(B) (bottom) in DCM after 4 successive irradiation cycles (2 min for each irradiation step in UV then 2 min in visible light). The pristine state is given at t0. Note that t2 curve is almost not visible here because superimposed on t0 and t4. In the insert at the top right is the absorbance of TPT(A) at 600 nm measured after several irradiation cycles.*

Section 4. Spectroscopic ellipsometry.

We recorded spectroscopic ellipsometry data (on *ca.* 1 cm^2 samples) in the visible range using a UVISEL (Horiba Jobin Yvon) spectroscopic ellipsometer equipped with DeltaPsi 2 data analysis software. The system acquired a spectrum ranging from 2 to 4.5 eV (corresponding to 300−750 nm) with intervals of 0.1 eV (or 15 nm). For the measurement in air (SAMs on Au), data were taken at an angle of incidence of 70°, and the compensator was set at 45°. We fit the data by a regression analysis to a film-on-substrate model as described by their thickness and their complex refractive indexes. First, a background for the substrate before monolayer deposition was recorded. We acquired three reference spectra at three different places of the surface spaced of few mm.dSecondly, after the monolayer deposition, we acquired once again three spectra at three different places of the surface and we used a 2-layer model (substrate/SAM) to fit the measured data and to determine the SAM thickness. We employed the previously measured optical properties of the substrate (background), and we fixed the refractive index of the organic monolayer at 1.50.[13] We note that a change from 1.50 to 1.55 would result in less than a 1 Å error for a thickness less than 30 Å. The three spectra measured on the sample were fitted separately using each of the three reference spectra, giving nine values for the SAM thickness. We calculated the mean value from this nine thickness values and the thickness incertitude corresponding to the standard deviation. Overall, we estimated the accuracy of the SAM thickness measurements at ± 2 Å.[14] For SAM on Co using the cell filled with N_2, data were taken at an angle of incidence of 60 ± 1° while the compensator was set at 45°. However, due to the rough Co surface and the use of the cell, the fits with a fixed angle of incidence at 60°C systematically give low values of thicknesses. The fits with this angle as an

additional fit parameter give higher values. Consequently, the thicknesses are given with a larger uncertainty (error bar) compared to SAM on Au.

Section 5. XPS measurements.

High resolution XPS spectra were recorded with a monochromatic $Al_{K\alpha}$ X-ray source ($h\upsilon$ = 1486.6 eV), a detection angle of 45° as referenced to the sample surface, an analyzer entrance slit width of 400 µm and with an analyzer pass energy of 12 eV. In these conditions, the overall resolution as measured from the full-width half-maximum (FWHM) of the Ag 3d5/2 line is 0.55 eV. Background was subtracted by the Shirley method.[15] The peaks were decomposed using Voigt functions and a least squares minimization procedure. Binding energies were referenced to the C 1s BE, set at 284.8 eV.

TPT(A) and TPT(B) SAMs on ^{TS}Au.

The C 1s peak at 284.8 eV (Fig. S3) corresponds to C-C, C-N and C-S bonds. The shoulder observed at 286.2 eV is assigned to the three C=N-S bonds.[16] The S 2p region shows two doublets (S $2p_{1/2}$ and S $2p_{3/2}$) associated to the S-C (S $2p_{1/2}$ at 165.4 eV, S $2p_{3/2}$ at 164.3 eV) and S-Au (S $2p_{1/2}$ at 162.9 eV, S $2p_{3/2}$ at 161.8eV) bonds (Fig. S3). These doublets are separated by 1.2 eV as expected with an amplitude ratio [S $2p_{1/2}$]/[S $2p_{3/2}$] of 1/2. The amplitude ratios [S-Au]/[S-C] are 0.42 for TPT(A) and 0.5 for TPT(B), slightly higher than the 1/3 expected ratio. A small peak at higher energy (≈ 168 eV) is associated to oxidized sulfur (SO_x). For both molecules, the N 1s region (Fig. S5) shows two peaks corresponding to "pyridine-like" nitrogen (C=N) and "coordinated-like" nitrogen (C=N**...**Au) at 398.6 eV and 400 eV, respectively.[17] The piridinic and coordinated-like designations are often used in the literature to describe the components of N 1s signals in N-doped carbons.[18] This N 1s peak splitting is observed when the N atoms interact with a metal surface.[19] The ratio of the peak amplitudes [C=N**...**Au]/[N=C] is

higher for TPT(B) (see Table S1) than for TPT(A) indicating that more N atoms are interacting with the metal electrode for TPT(B) SAM than for the TPT(A) SAM.

TPT(A) and TPT(B) SAMs on Co.

The XPS spectra of TPT(A) and TPT(B) on Co show all the C, N and S elements. As for the molecules on ^{TS}Au, the major peak at 284.8 eV is composed of C-C, C-N and C-S components and a shoulder observed at 286.2 eV is assigned to the three S-C=N carbons (Fig. S4). In the S 2p region (Fig. S4), we observe the contribution of S-C and S-Co bonds (S $2p_{3/2}$ at 164.3 eV, S $2p_{1/2}$ at 165.4 eV for S-C and S $2p_{1/2}$ at 163.7 eV, S $2p_{3/2}$ at 162.6 eV for S-Co). As for the SAMs on Au, the amplitude ratios [S-Co]/[S-C] ~ 0.5-0.6 are higher than the expected 1/3 ratio. Albeit the protocol and precautions used during the grafting and measurements, the O 1s region reveals a residual oxidized Co[20] as in our previous work on azobenzene derivatives on Co (Fig. S3 in Ref. 21). The N 1s region (Fig. S5) shows the two peaks of the C=N bonds (398.6 eV) and the C=N**...**Co one (400 eV)[17] with ratios of amplitude [C=N**...**Co]/[N=C] larger for the TPT(B) than for TPT(B) molecules (Table S1). As for the SAMs on Au, this may be due to interaction of N with the surface (large molecule tilt). However, we have also observed (in another batch #2) a case with a low [C=N**...**Co]/[N=C] ratio which was inferred to a "non tilted" molecule configuration (see discussion section in the main text) for which the N atoms are away from the surface and consequently, only the pyridinic form N=C is detected by XPS.

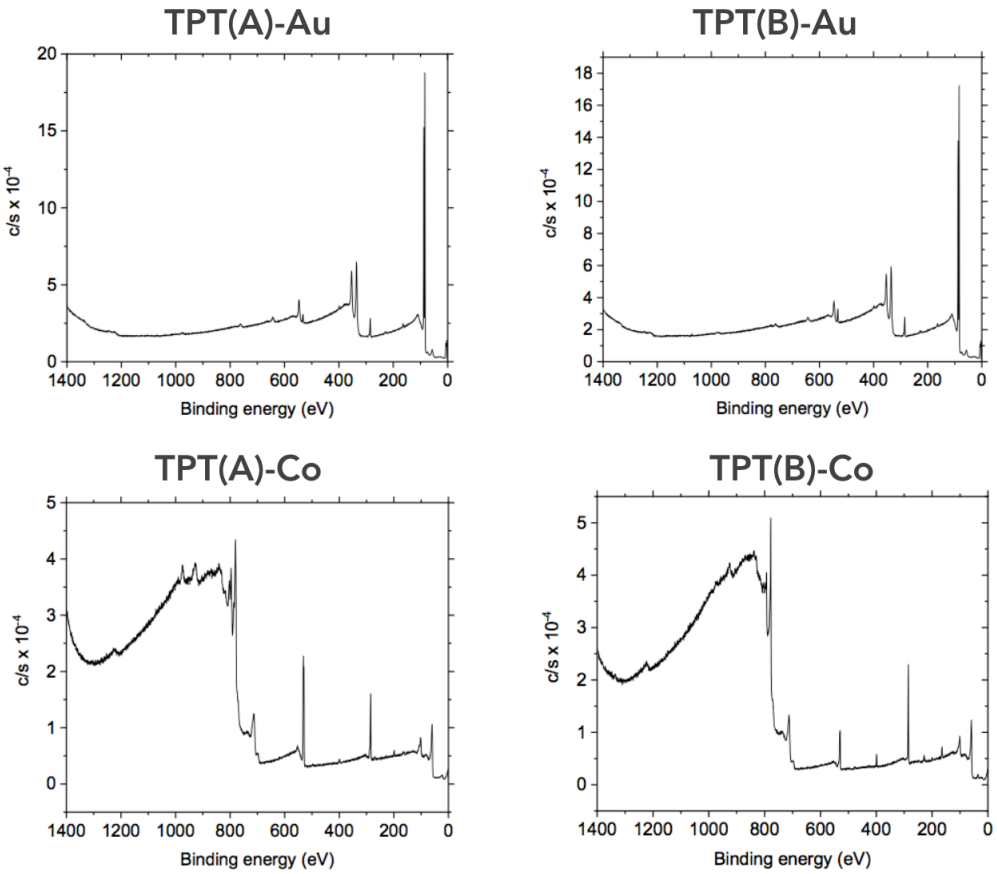

Figure S2. *XPS survey spectra of the TPT SAMs on Au and Co.*

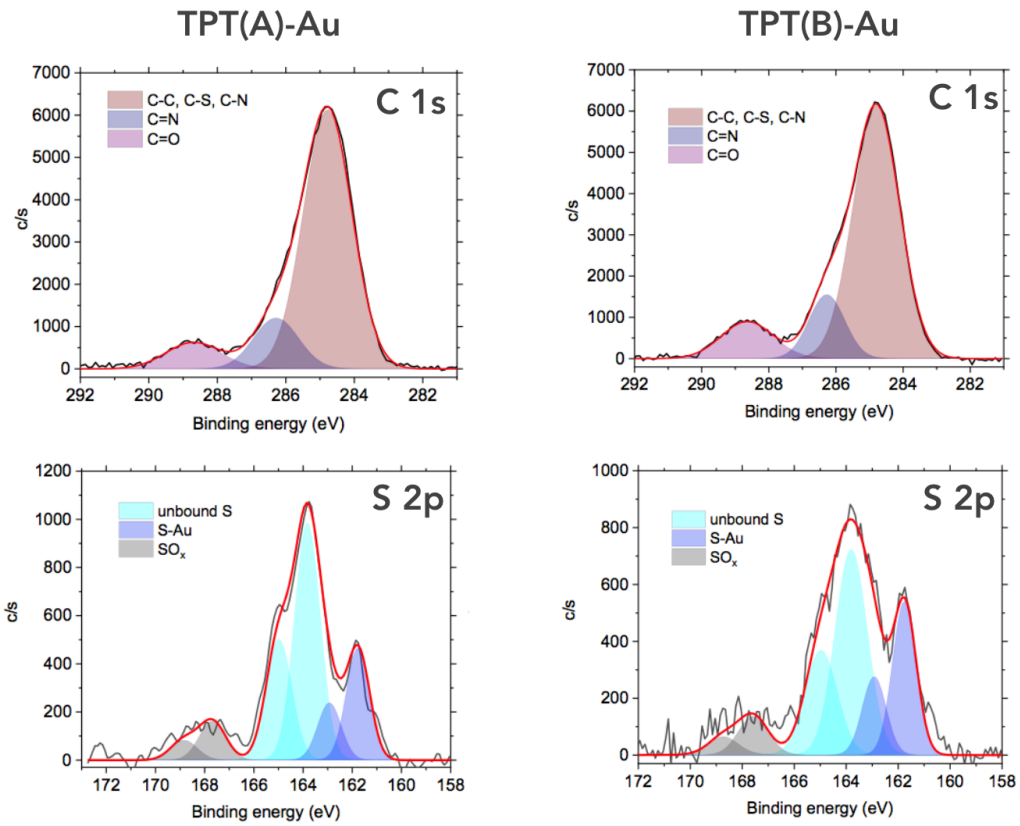

Figure S3. *XPS spectra of the TPT(A)-Au and TPT(B)-Au samples: C 1s and S 2p regions.*

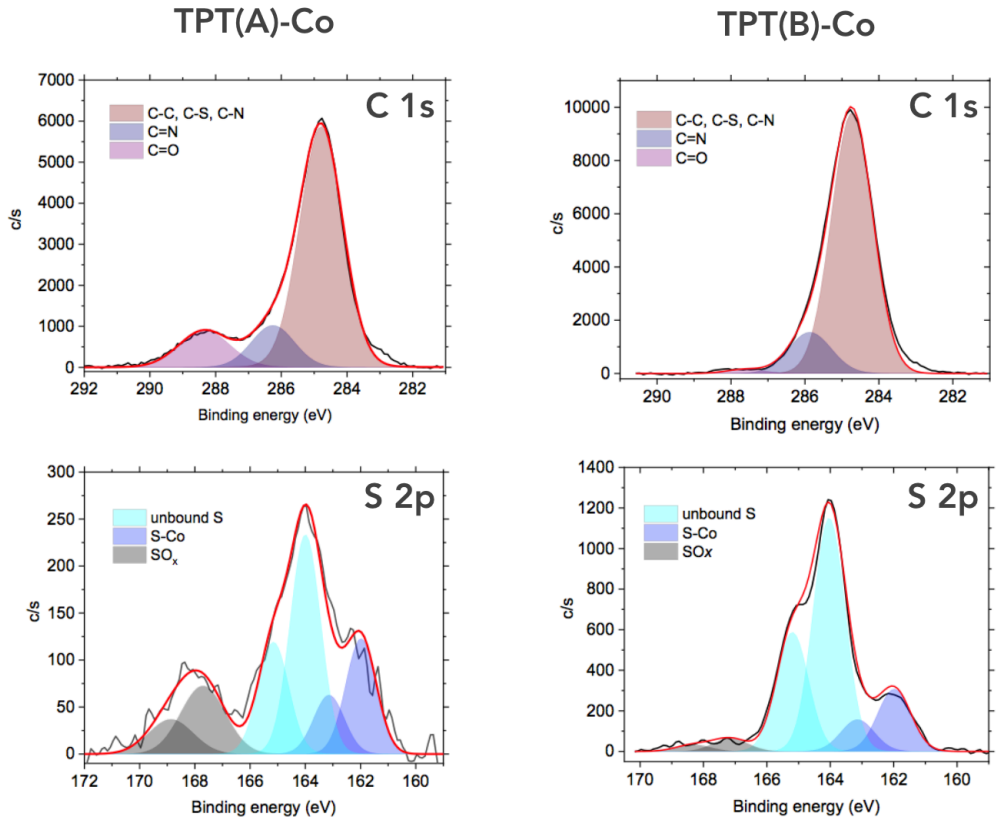

Figure S4. *XPS spectra of the TPT(A)-Co and TPT(B)-Co samples: C 1s and S 2p regions.*

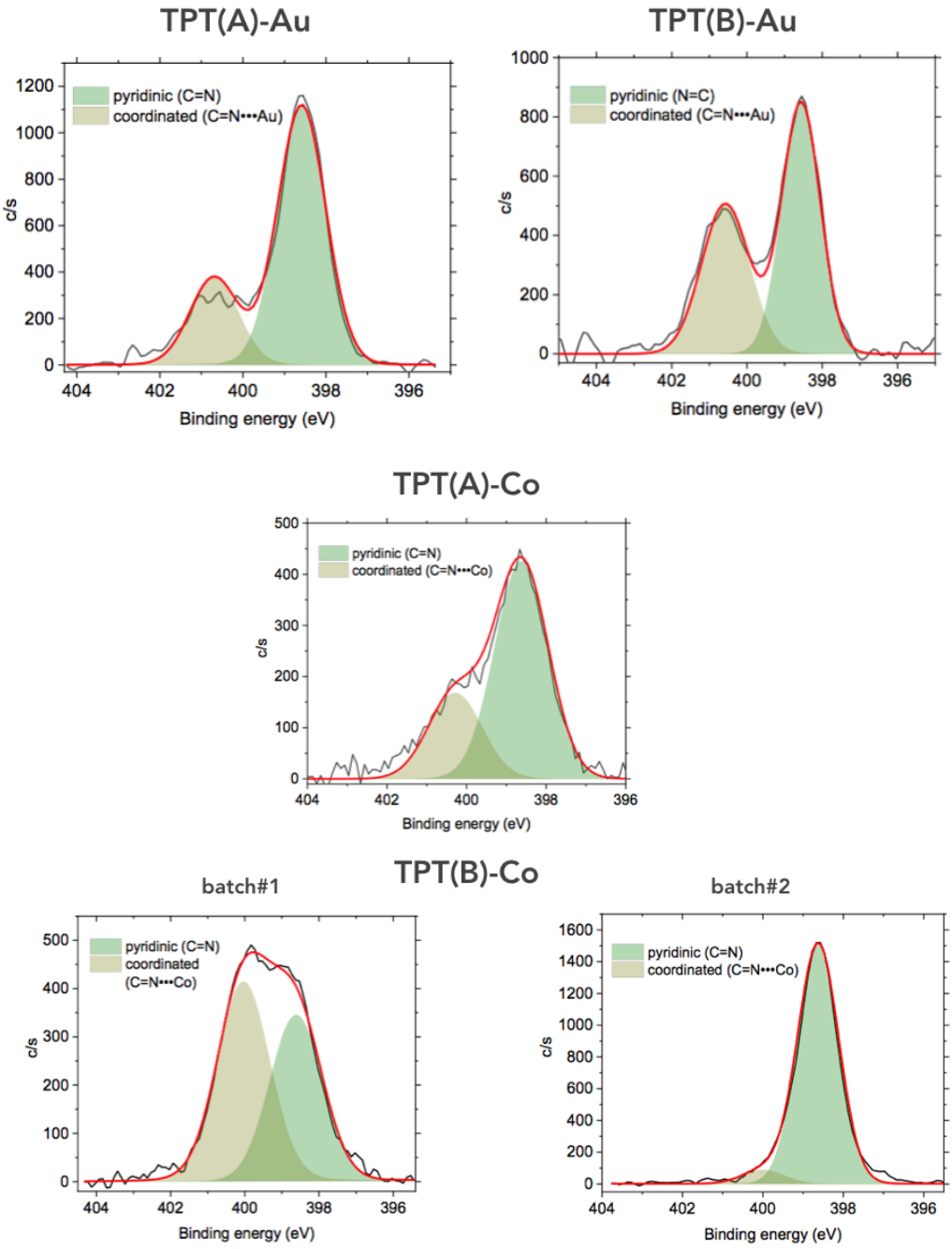

Figure S5. *XPS spectra of the TPT(A) and TPT(B) SAMs on Au and Co sample: N 1s regions.*

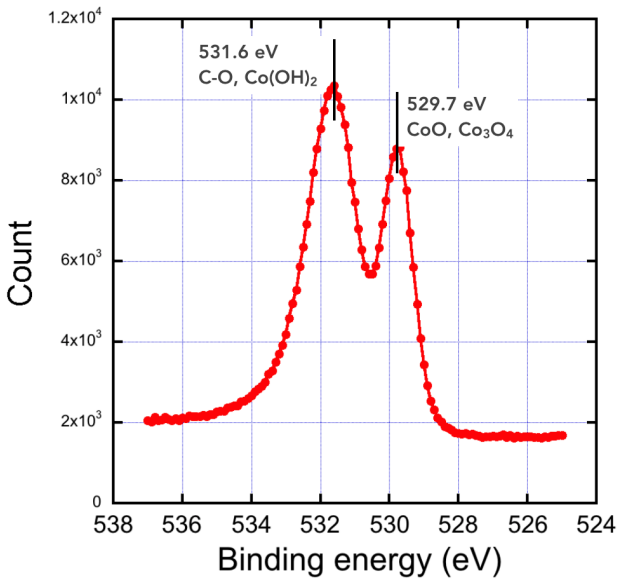

***Figure S6**. XPS spectra of theTPT(B) SAMs on Co sample: O 1s regions. The two peaks are mainly assigned to oxidized Co.[20]*

	Pyridinic-like Area	Coordinated-like Area	[C=N...M]/[N=C]	BE (eV)
TPT(A)-Au	1647	555	0.34	398.6, 400.7
TPT(B)-Au	1085	807	0.74	398.6, 400.6
TPT(A)-Co	719	283	0.39	398.6, 400.3
TPT(B)-Co #1	609	757	1.24	398.6, 400.0
TPT(B)-Co #2	1939	111	0.06	398.6, 400.0

***Table S1.** Area of the two N 1s peaks, ratio of the peak amplitude and binding energy of the two peaks (M = Au or Co).*

Section 6. CAFM measurements.

CAFM in air.

Current−voltage characteristics were measured by conductive atomic force microscopy (Icon, Bruker), using PtIr coated tip (SCM-PIC from Bruker, 0.2 N/m spring constant). To form the molecular junction, the conductive tip was located at a stationary contact point on the SAM surface at controlled loading force (~ 15 nN). The voltage was applied on the substrate. The CAFM tip is located at different places on the sample (typically on an array of stationary contact points spaced of 50-100 nm), at a fixed loading force and the I−V characteristics were acquired directly by varying voltage for each contact point. The I-V characteristics were not averaged between successive measurements and typically between few hundreds and a thousand I-V measurements were acquired on each sample.

CAFM in UHV.

CAFM in UHV (10^{-11} - 10^{-9} mbar) were carried out at room temperature with a VT-SPM microscope (Scienta Omicron) and using PtIr coated probes SCM-PIC-V2 (Bruker), tip radius R = 25 nm, spring constant k = 0.1 N/m. In all our measurements, bias (V) was applied on the substrate and the current was recorded with an external DLPCA-200 amplifier (FEMTO). Hundreds to thousands IV traces were acquired using the same protocol as for CAFM measurements in air.

Loading force and CAFM tip contact area.

The load force was set at ~ 15 nN for all the I-V measurements, a lower value leading to too many contact instabilities during the I-V measurements. Albeit larger than the usual load force (2-5 nN) used for CAFM on SAMs, this value is below the limit of about 60-70 nN at which the SAMs start to suffer from severe degradations. For example, a detailed study (Ref. 22) showed a limited strain-induced deformation of the monolayer (≲ 0.3 nm) at this used load force. The

same conclusion was confirmed by our own study comparing mechanical and electrical properties of alkylthiol SAMs on flat Au surfaces and tiny Au nanodots.[23]

Considering: (i) the area per molecule on the surface (as estimated for the thickness measurement and calculated geometry optimization - see theory section), and (ii) the estimated CAFM tip contact surface (see below), we estimate N as follows. As usually reported in literature[22, 24-26] the contact radius, a, between the CAFM tip and the SAM surface, and the SAM elastic deformation, δ, are estimated from a Hertzian model:[27]

$$a^2 = \left(\frac{3RF}{4E^*} \right)^{2/3} \quad \text{(S1)}$$

$$\delta = \left(\frac{9}{16R} \right)^{1/3} \left(\frac{F}{E^*} \right)^{2/3} \quad \text{(S2)}$$

with F the tip load force (15 nN), R the tip radius (25 nm) and E* the reduced effective Young modulus defined as:

$$E^* = \left(\frac{1}{E^*_{SAM}} + \frac{1}{E^*_{tip}} \right)^{-1} = \left(\frac{1-\nu^2_{SAM}}{E_{SAM}} + \frac{1-\nu^2_{tip}}{E_{tip}} \right)^{-1} \quad \text{(S3)}$$

In this equation, $E_{SAM/tip}$ and $\nu_{SAM/tip}$ are the Young modulus and the Poisson ratio of the SAM and C-AFM tip, respectively. For the Pt/Ir (90%/10%) tip, we have E_{tip} = 204 GPa and ν_{tip} = 0.37 using a rule of mixture with the known material data.[28] These parameters for the DAE SAM are not known and, in general, they are not easily determined in such a monolayer material. Thus, we consider the value of an effective Young modulus of the SAM E^*_{SAM} = 38 GPa as determined for the "model system" alkylthiol SAMs from a combined mechanic and electron transport study.[22] With these parameters, we estimate a = 2 - 2.6 nm (contact area = 13.2 - 21 nm²) and δ = 0.16 - 0.26 nm. With a molecular packing density between 1 to 2 nm²/molecule (as estimated from the tilt angle and theoretical

configuration optimization, see theory section), we infer that about 10 molecules are measured in the TPT/PtIr junction, thus we used N=10 in all the I-V fit using Eq. 1 (main text).

Data analysis.

Before to construct the current histograms and fit the I-V curves with the one energy-level model, the raw set of IV data is analyzed and some I-V curves were discarded from the analysis:

- At high current, the I-V traces that reached the saturating current during the voltage scan (the compliance level of the trans-impedance amplifier, typically $5x10^{-9}$ A in Figs. S6 and S7, depending on the gain of the amplifier) and/or I-V traces displaying large and abrupt steps during the scan (contact instabilities).
- At low current, the I-V traces that reached the sensitivity limit (almost flat I-V traces) and displayed random staircase behavior (due to the sensitivity limit of both the trans-impedance amplifier and the resolution of the ADC (analog-digital converter), Fig. S7. A typical example of such treatment is shown in Fig. S6. The "measurement yield" for the four samples is summarized in Table S2.

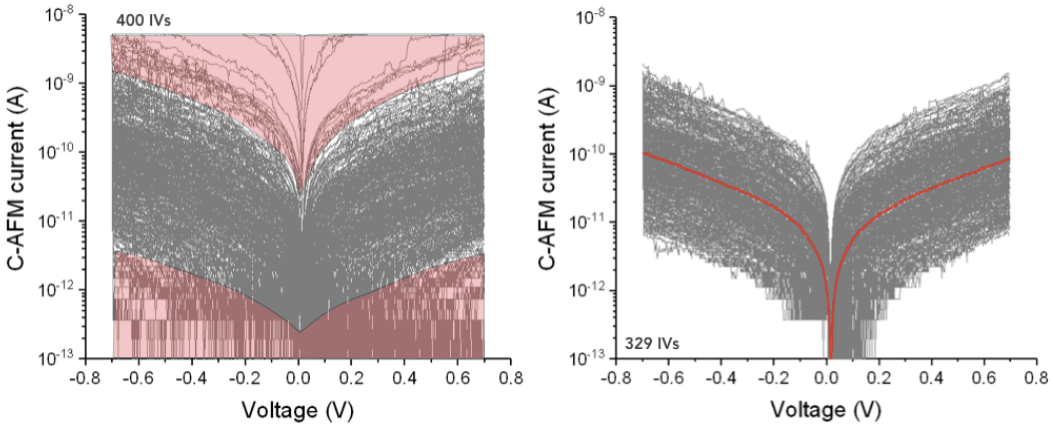

Figure S7. *Comparison of the complete set of I-V traces (400 IVs) measured on the TPT(A)-Au pristine sample. The light red areas show the IVs traces discarded (see text) from the analysis, leading to 329 useful IVs.*

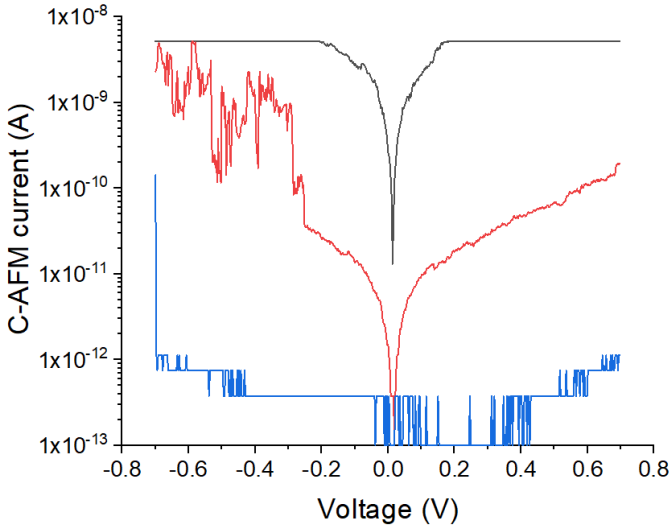

Figure S8. *Typical examples of I-V curves discarded from the data analysis.*

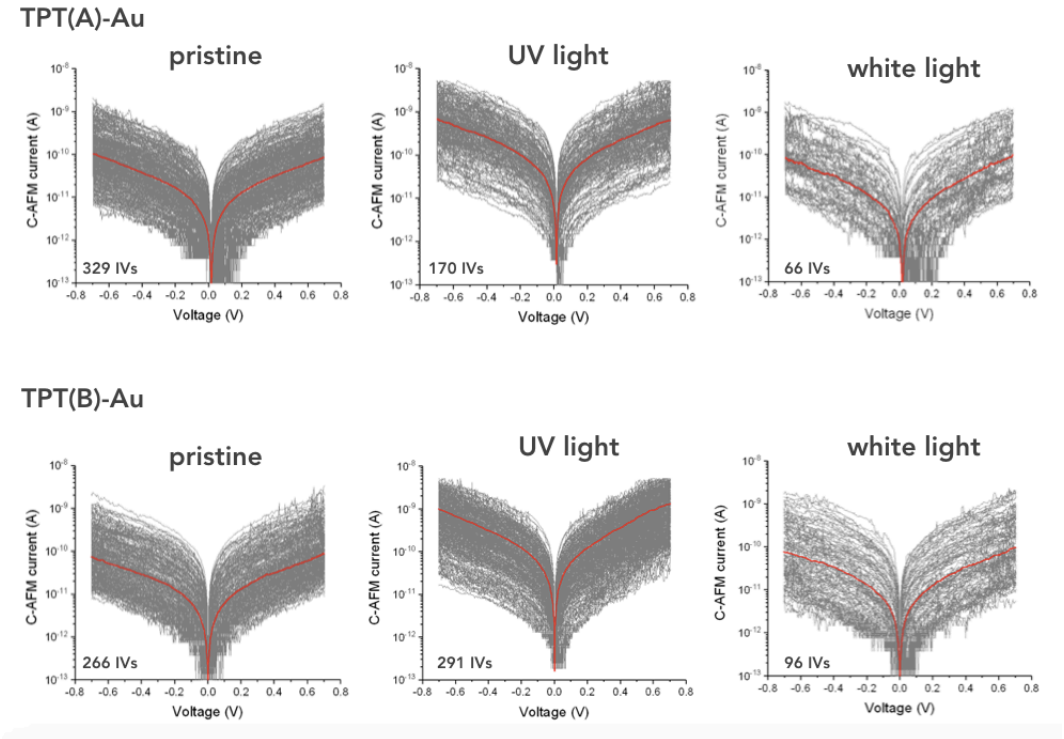

Figure S9. *Datasets of the I-V measurements (semi-log scale) for the Au-TPT(A) and TPT(B) SAMs (pristine, after UV light illumination and visible light illumination). The red lines are the mean Ī-V curves.*

	Complete set	Analyzed set
Au-TPT(A) pristine/UV/vis	400/400/400	329/170/66
Au-TPT(B) pristine/UV/vis	400/400/400	266/291/96
Co-TPT(A) pristine/UV/vis	400/400/400	141/364/185
Co-TPT(B) pristine/UV/vis	625/1250/625	225/514/107

Table S2. *Measurement yield.*

Voltage dependent $R_{c/o}$.

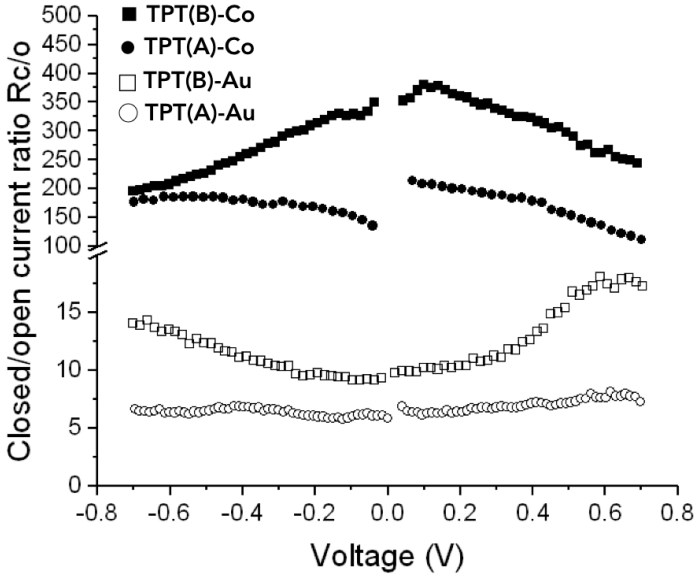

Figure S10. *Closed/open current ratio versus voltage $R_{c/o}(V)=\bar{I}_{UV}(V)/\bar{I}_{pristine}(V)$ for the four samples.*

Fit of the energy level model.

All the I-V traces in Figs. 3-4 (main text) were fitted individually with the single energy-level (SEL) model (Eq. 1, main text) with 3 fit parameters: ε_0 the energy

position (with respect to the Fermi energy of electrodes) of the molecular orbital involved in the electron transport, Γ_1 and Γ_2 the coupling energy between the molecules and the two electrodes. The fits were done with the routine included in ORIGIN software, using the method of least squares and the Levenberg Marquardt iteration algorithm.

The SEL model is a low temperature approximation albeit it can be used at room temperature for voltages below the resonant transport conditions[29, 30] since the temperature broadening of the Fermi function is not taken into account. Moreover, a possible voltage dependance of ε_0 is also neglected.[31] It is known that the value of ε_0 given by the fit of the SEL model depends on the voltage window used for the fit.[29-31] This feature is confirmed (Fig. S10) showing that unreliable values are obtained with a too low voltage range (i.e. the SEL model is not reliable in the linear regime of the I-V curves) and not applicable when the voltage is high enough to bring the electrode Fermi energy close to molecular orbital (near resonant transport), here for a voltage window -0.7/0.7 V where all the values of ε_0 collapse. In the voltage windows -0.3/0.3 V to -0.6/0.6V we clearly observe a lowering of ε_0 upon UV illumination by around 0.1 eV for TPT(A) and 0.13 eV for TPT(B) - on average, a behavior also confirmed by the TVS (transient voltage spectroscopy) method (*vide infra*, Fig. S11).[32-37] For these reasons we limited the fits to a voltage window -0.5 V to 0.5 V to analyze the complete datasets shown in Figs. 3 - 4 (main text). To construct the histograms of the values of ε_0, Γ_1 and Γ_2 (Figs. 6 and 7), we discarded the cases for which the fits were not converging of not accurate enough (i.e. R-squared < 0.95). Typical fits on the mean $\bar{I}$-V curves are shown in Fig. S11 for the two samples on ^{TS}Au and the three conditions (pristine, after UV light, after white light).

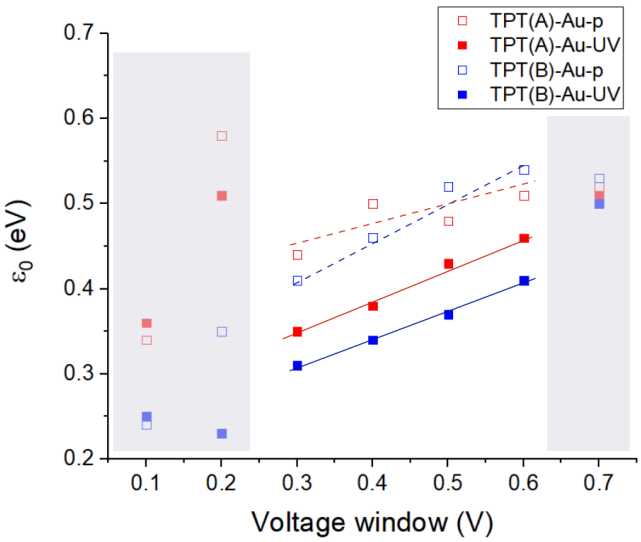

Figure S11. *Values of ε_0 obtained with SEL model fitted on the mean $\bar{I}$-V curves for the two molecules on ^{TS}Au (pristine and after UV illumination) with increasing voltage windows (-0.1/0.1 V to -0.7/0.7 V) for the fits.*

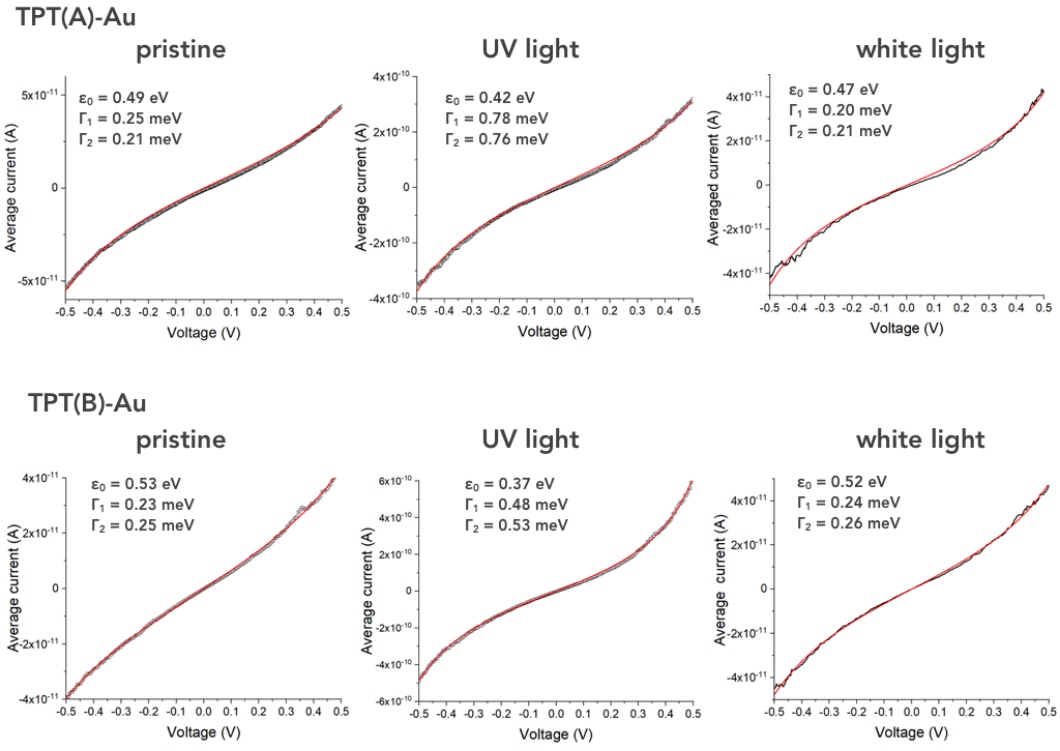

Figure S12. *One energy level model fits on the mean current-voltage curves.*

The same mean Ī-V curves are also analysed by TVS, plotting V^2/I (in absolute value) versus V (Fig. S12),[38] and determining the transition voltages (V_{T+} and V_{T-}) for both voltage polarities, i.e. the voltage at the maximum of V^2/I. This threshold voltage indicates the transition between off-resonant (below V_T) and resonant (above V_T) transport regime in the molecular junctions. The values of ε_0 are estimated by:[36]

$$\left|\varepsilon_0\right| = 2\frac{e\left|V_{T+}V_{T-}\right|}{\sqrt{V_{T+}^2 + 10\left|V_{T+}V_{T-}\right|/3 + V_{T-}^2}} \qquad \text{(S4)}$$

and they are marked in Fig. S12. They are in good agreement with the SEL fits (Fig. S11).

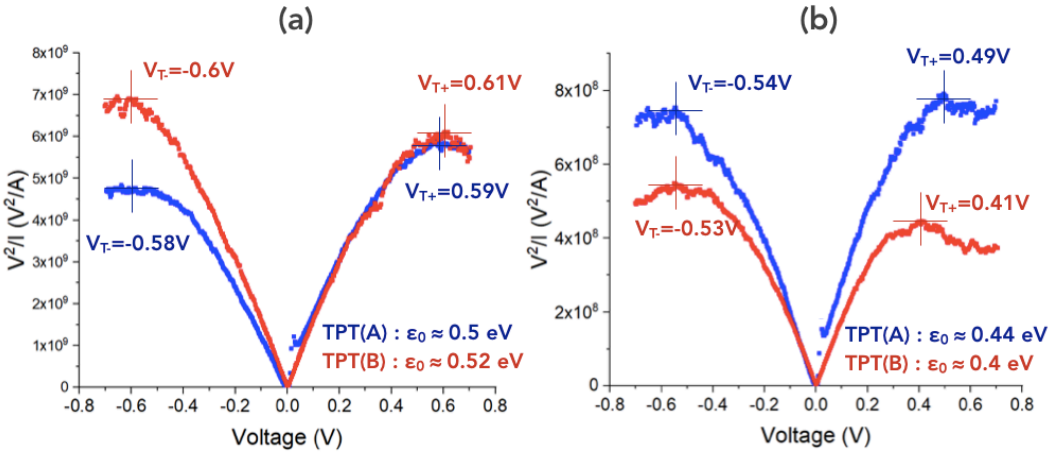

Figure S13. *Typical TVS plots ($|V^2/I|$) vs. V. (a) TPT(A)-Au (blue) and TPT(B)-Au (red) in the pristine sate (open), (b) same samples after UV illumination (closed state). The thresholds V_{T+} and V_{T-} are indicated by the cross (with value) as well as the estimated values of ε_0 using Eq. (S4).*

Section 7. Illumination setup.

We used a power LED (M365FP1 from Thorlabs) for UV light irradiation (CAFM in air). This LED has a wavelength centered at 365 nm (close to the absorbance

peak, see Fig. S1) and a bandwidth of 8 nm. An optical fiber was brought close (ca. 1 cm) to the sample in the CAFM setup (optical power density at the sample location ca. 27 mW/cm^2). A chromatographic UV lamp (Vilbert-Lourmat, with a sharp peak at 365 nm and a background centered at 350 nm, BWHM: ~330-370 nm) was used for the measurements with the UHV CAFM and the irradiation of the sample was performed in the entry lock (P = 10^{-6} mbar N_2) of the instrument (optical power density at the sample location, ca. 10 cm is ca. 0.65 mW/cm^2). For the visible light irradiation, we used a white light halogen lamp (Leica CLS150X) with a bandwidth centered at 600 nm (BWHM: ~500-700 nm), matching the absorbance peak of the closed form of TPT (Fig. S1) (optical power density at the sample location: ca. 220 mW/cm^2 in air at ca. 1 cm and ca. 13 mW/cm^2 at 10 cm for the experiments in UHV). Under these conditions, the samples were exposed to light for 1-3 h in air and 10-15 h in UHV, corresponding to almost the same photon density received by the sample, typically ~ 10^{20} photons/cm^2. These conditions correspond to photostationnary states and we did not observe significant CAFM current variations with longer duration of light exposure.

Section 8. Theoretical methods and additional calculations.

Simulated I-V curves.

The I-V characteristics have been calculated on the basis of the Landauer-Büttiker formalism, which links the transmission spectrum to the current in a coherent transport regime.[39] When a bias is applied, the current is calculated via the integration of the transmission spectrum within a bias window defined by a Fermi-Dirac statistics in the left and right electrodes:

$$I(V) = \frac{2e}{h}\int T(E)\left[f\left(\frac{E-\mu_R}{k_B T_R}\right) - f\left(\frac{E-\mu_L}{k_B T_L}\right)\right]dE \qquad \text{(S5)}$$

where T(E) is the transmission spectrum, E the incident electron energy, f the Fermi function, $\mu_{R/L}$ the chemical potential of the right/left electrode, $T_{R/L}$ the

temperature of the right/left electrode set here to 300K, k_B the Boltzmann constant, e the elementary charge, h the Planck constant and V the applied bias. It is important to note that for an accurate estimation of the current, the transmission spectrum T(E) should be calculated in a self-consistent way for each bias. Thus, the current-voltage properties and the $R_{c/o}$ of the Au-TPT/Au junctions were predicted by using the transmission calculated at each bias, which is not too probihitive at the computational level. However, it is possible to obtain a reasonable approximation for the current at low bias by using the transmission spectrum at zero bias. This approximation is required for Co-TPT/Au junctions with a large unit cell and a spin-polarized electrode because the self-consistent calculations become very time consuming. Accordingly, the current-voltage properties of Co-PTP/Au and the corresponding $R_{c/o}$ were predicted by using the transmission calculated at zero bias.

Lorentzian fitting: Γ broadening of Au-TPT(A)/Au junction transmission peaks.

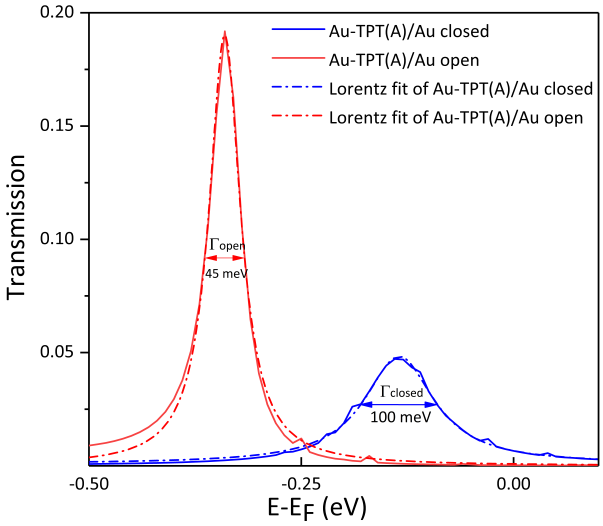

Figure S14. *Lorentzian fitting of the transmission peak of Au-TPT(A)/Au junction in both closed and open forms. The fitted Γ marked by an arrow indicates that the closed form exhibits larger broadening (100 meV) compared to open form (45 meV).*

Au-TPT/Au molecular junctions : non tilted configuration.

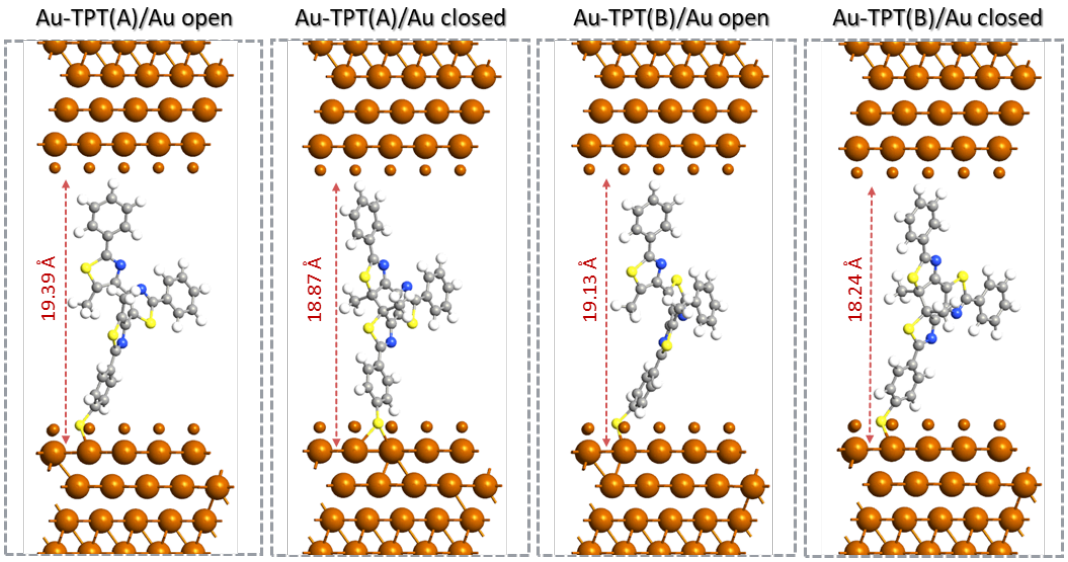

Figure S15. *Optimized Au-TPT/Au junctions in a non tilted configuration. The calculated junction thickness is also marked. The small brown atoms refer to the gold ghost atoms.*

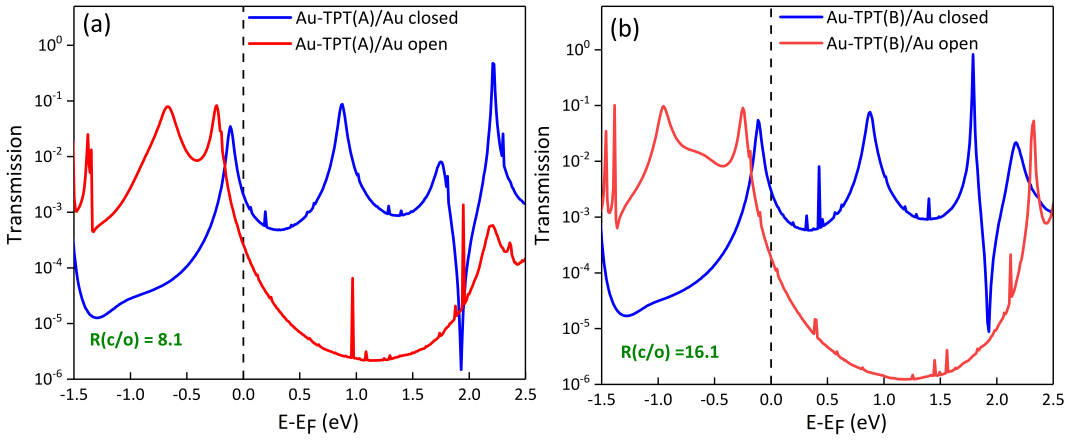

Figure S16*. Log scale plot of the transmission spectra at zero bias for non tilted (a) Au-TPT(A)/Au and (b) Au-TPT(B)/Au junctions in their closed and open forms. The calculated* $R_{c/o}$ *are 8.1 and 16.1, respectively.*

HOMO evolution as a function of the bias for Au-TPT/Au junctions.

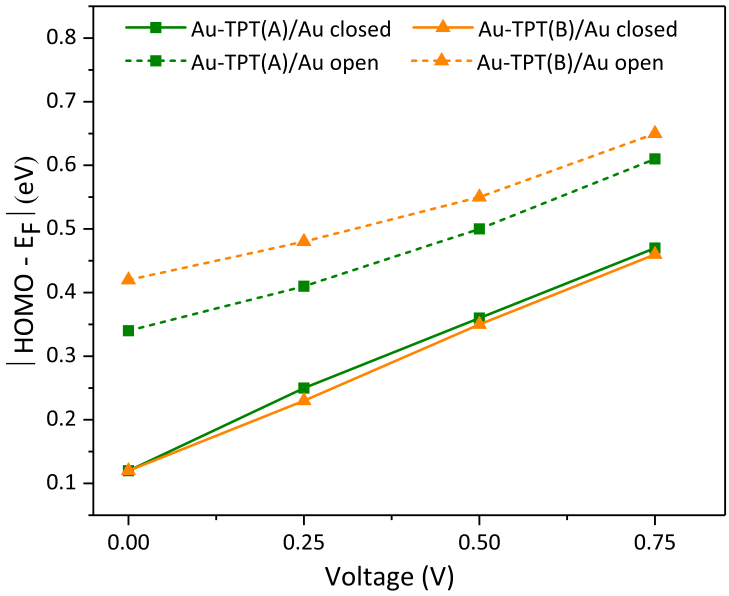

Figure S17. *The HOMO level evolution with respect to the average Fermi level of the electrodes as a function of the bias.*

Charge transfer at the interface.

The charge rearrangement upon bond formation between the metal surface and the molecule[40] is defined as the difference between the plane averaged charge density of the full metal-SAM system, ρ_{sys} and the sum of the density of the isolated subsystems, the free metal surface ρ_{slab} and the free-standing molecules ρ_{SAM}:

$$\Delta\rho(z) = \rho_{sys} - \rho_{slab} - \rho_{SAM} \quad \text{(S6)}$$

For a deeper understanding of the implications of the charge rearrangements at the metal-SAM interface, we calculate the net charge transfer at the interface (ΔQ) by integrating the charge density redistribution (Δρ) along the z normal axis.

$$\Delta Q(z) = \int_0^z \Delta\rho(z)dz \quad \text{(S7)}$$

This gives the total amount of charge transferred from the left to the right of a plane lying at the position z. Here, the electronic density of the free metal surface (the isolated molecule) is calculated by removing the molecule (metal surface) from the functionalized system while keeping the same geometry as in the full system. Note that we describe here the chemisorption process in a radical scenario depicting the formation of a covalent bond between the molecule in its radical form and the metal surface.[40-42]

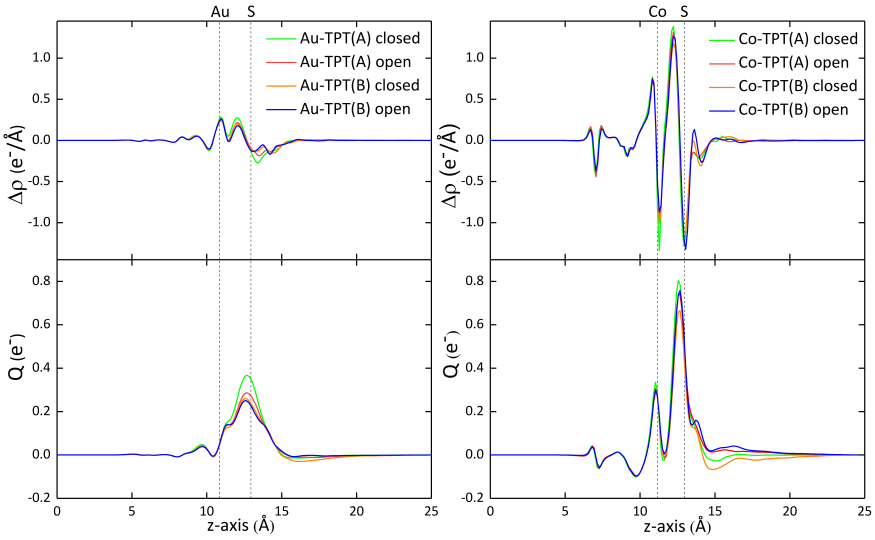

Figure S18. *Plane averaged charge density (top) and cumulative charge transfer (bottom) along the normal axis to the metal surface for Au-TPT (left) and Co-TPT(right). The dashed straight vertical lines represent the position of the first Au (Co) layer and S anchoring atom.*

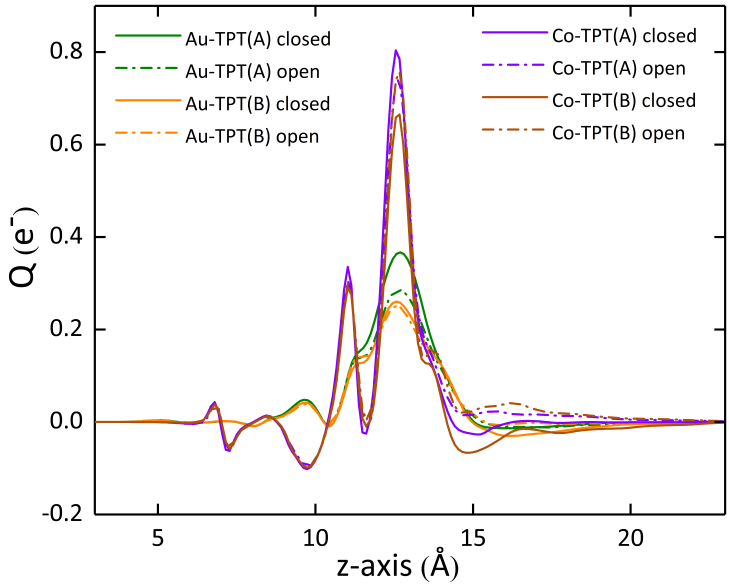

***Figure S19**. Cumulative charge transfer along the normal axis to the metal surface for Au-TPT versus Co-TPT SAMs. The net charge transfer between the metal surface and TPT molecules is significantly larger for Co-TPT SAMs compared to Au-TPT SAMs.*

Spin-dependent transmission spectra.

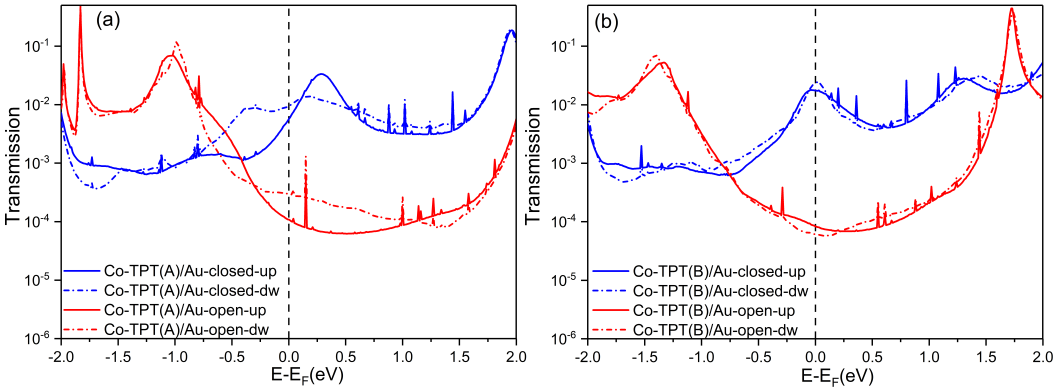

***Figure S20.** Log scale plot of the spin up (solid line) and spin down (dashed line) transmission spectra at zero bias for (a) Co-TPT(A)/Au and (b) Co-TPT(B)/Au junctions in their closed and open forms.*

Zero-bias vs. finite bias voltage transmission spectra.

We have calculated the closed/open ratio for Au-TPT/Au systems on the basis of the zero transmission spectra (see Table S3 below).

	Au-TPT(A)/Au		Au-TPT(B)/Au	
Bias (V)	Finite-bias	Zero transmission	Finite-bias	Zero transmission
0	26.5	26.5	69.1	69.1
0.25	19.7	28.0	63.8	115
0.5	20	6.6	52	54
0.75	43.8	0.8	86.2	5

Table S3. *Closed/open ratios ($R_{c/o}$) for the Au-TPT(A)/Au and Au-TPT(B)/Au junctions calculated using voltage-dependent transmission spectra (finite-bias) versus the zero-bias transmission spectra.*

By using the zero transmission spectrum, we obtain the same trend as with the finite-bias calculations: the Au-TPT(B) exhibits higher closed/open ratio compared to Au-TPT(A). However, the discrepancy associated t the use of the zero transmission spectra for estimating the closed/open ratio magnitude is sensitive to the voltage and the studied system (TPT(A) or TPT(B)), with a reasonable agreement found at 0.25V and 0.5V between the two options. We could then conclude it is reasonable to use the zero-bias transmission to compare with experimental results measured at 0.5V.

However, we consider these results obtained for a gold substrate are not directly transferrable to cobalt substrates. In fact, the TPT molecules exhibit a stronger coupling to cobalt that could result in a very different voltage drop. In other words, the magnitude of the discrepancy between the zero and the non-equilibrium transmissions highly depends on the investigated junction.

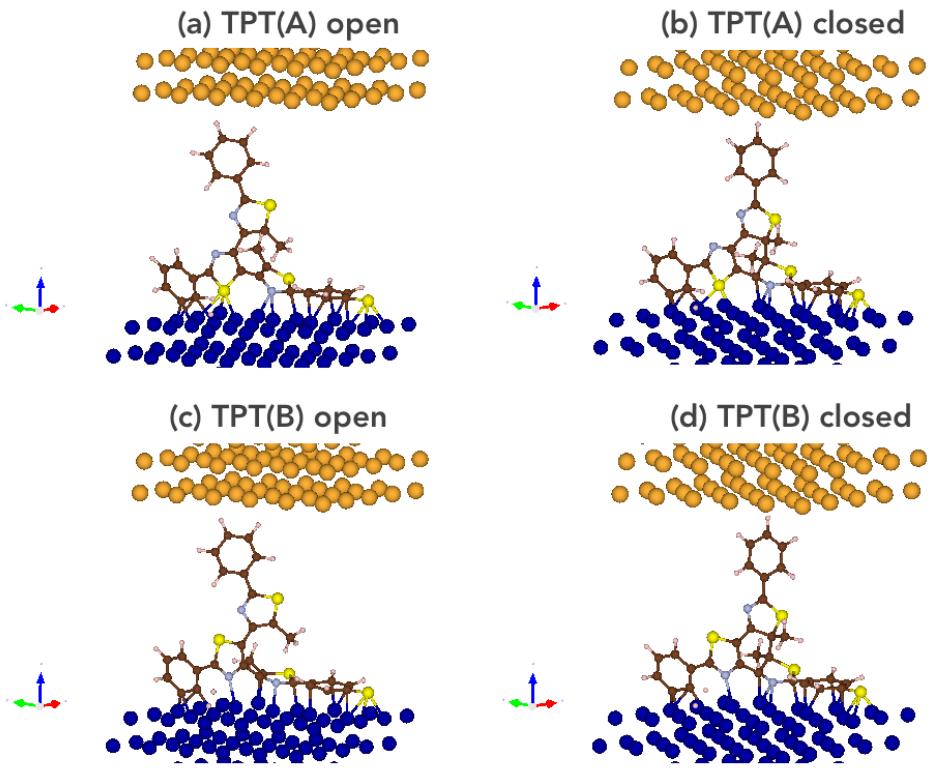

Figure S21. *Closer view of Co-TPT interfaces: (a) and (b) TPT(A) molecule with only one N atom of the thiazole interaction with the Co surface, (c) and (d) TPT(B) molecule with 2 N atoms of the thiazole units interacting with the Co surface.*

Co-TPT/Au molecular junctions: non tilted configuration.

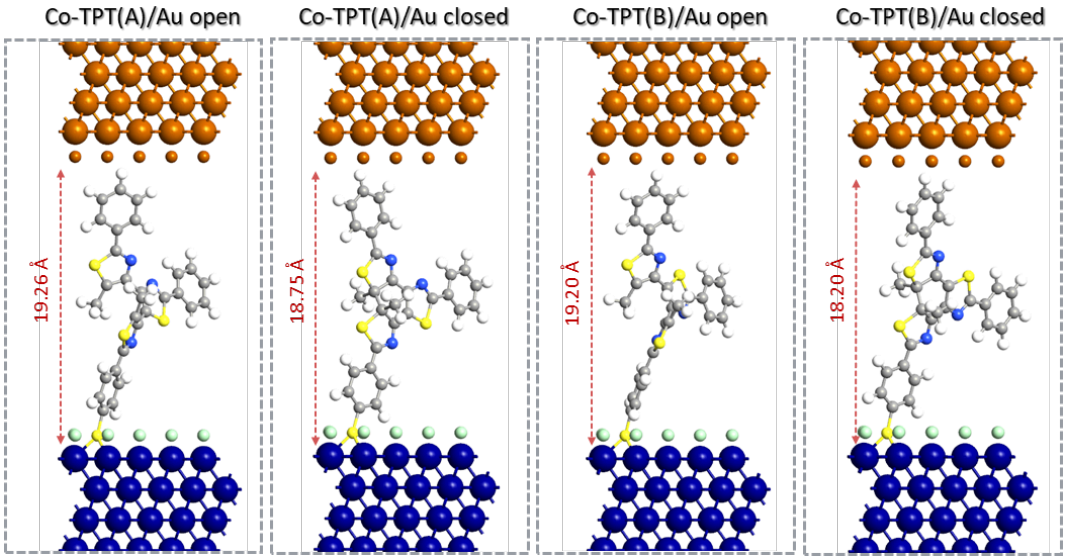

Figure S22. *Optimized non tilted Co-TPT/Au junctions. The calculated junction thickness is also marked. The small brown (green) atoms refer to gold (platinum) ghost atoms.*

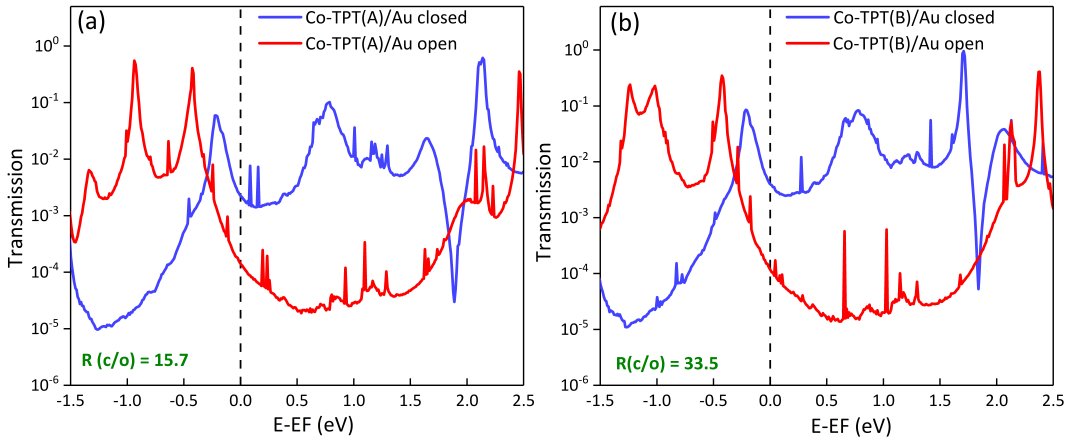

Figure S23. *Log scale plot of the transmission spectra at zero bias for non tilted (a) Co-TPT(A)/Au and (b) Co-TPT(B)/Au junctions in their closed and open forms. The calculated $R_{c/o}$ are 15.7 and 33.5, respectively.*

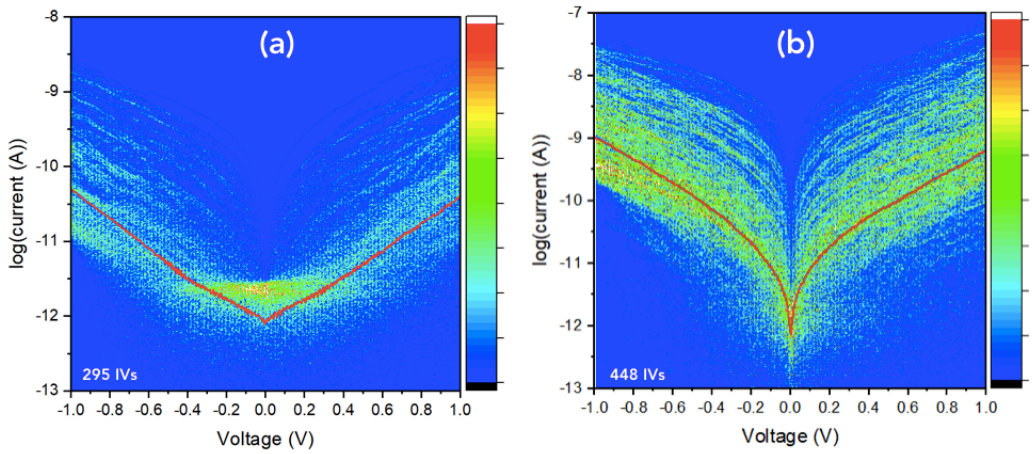

Figure S24. *2D histograms of the current-voltage (I-V) curves: (a) pristine SAM of TPT(B) on Co (batch #2), (b) after UV irradiation. The currents are measured by CAFM in UHV. The number of I-V traces in the dataset are shown on the figures. The red line is the mean* $\bar{I}$ *current. From the mean current, the ratio* $R_{c/o}$ *is 15-25.*

References

1. Li, X.; Li, C.; Yin, B.; Li, C.; Liu, P.; Li, J.; Shi, Z. *Chemistry – An Asian Journal* **2013,** 8, (7), 1408-1411.
2. Hämmerle, J.; Schnürch, M.; Stanetty, P. *Synlett* **2007,** 2007, (19), 2975-2978.
3. Holzweber, M.; Schnürch, M.; Stanetty, P. *Synlett* **2007,** 2007, (19), 3016-3018.
4. Hashimoto, Y.; Nakashima, T.; Shimizu, D.; Kawai, T. *Chem Commun* **2016,** 52, (29), 5171-5174.
5. Ouhenia-Ouadahi, K.; Yasukuni, R.; Yu, P.; Laurent, G.; Pavageau, C.; Grand, J.; Guérin, J.; Léaustic, A.; Félidj, N.; Aubard, J.; Nakatani, K.; Métivier, R. *Chem Commun* **2014,** 50, (55), 7299-7302.
6. Stuhr-Hansen, N. Synthetic Communications **2003,** 33, (4), 641-646.

7. Schnürch, M.; Hämmerle, J.; Mihovilovic, M. D.; Stanetty, P. *Synthesis* **2010,** 2010, (05), 837-843.

8. Gavrel, G.; Yu, P.; Léaustic, A.; Guillot, R.; Métivier, R.; Nakatani, K. *Chem Commun* **2012,** 48, (81), 10111-10113.

9. Weiss, E.; Chiechi, R.; Kaufman, G.; Kriebel, J.; Li, Z.; Duati, M.; Rampi, M.; Whitesides, G. *J. Am. Chem. Soc* **2007,** 129, (14), 4336-4349.

10. Weiss, E. A.; Kaufman, G. K.; Kriebel, J. K.; Li, Z.; Schalek, R.; Whitesides, G. M. *Langmuir* **2007,** 23, (19), 9686-9694.

11. Tour, J. M.; Jones, L.; Pearson, D. L.; Lamba, J. J. S.; Burgin, T. P.; Whitesides, G. M.; Allara, D. L.; Parikh, A. N.; Atre, S. *J Am Chem Soc* **1995,** 117, (37), 9529-9534.

12. Vaughan, O. P. H.; Turner, M.; Williams, F. J.; Hille, A.; Sanders, J. K. M.; Lambert, R. M. *J Am Chem Soc* **2006,** 128, (30), 9578-9579.

13. Ulman, A., An introduction to ultrathin organic films : from Langmuir-Blodgett to Self-assembly. Academic press: Boston, 1991.

14. Rabe, J. P.; Knoll, W. *Optics Communications* **1986,** 57, (3), 189-192.

15. Shirley, D. A. *Phys. Rev. B* **1972,** 5, 4709-4714.

16. Xiao, J.; Liu, Z.; Zhang, W.; Deng, N.; Liu, J.; Zhao, F. *Molecules* **2021,** 26, (22), 7039.

17. Osadchii, D. Y.; Olivos-Suarez, A. I.; Bavykina, A. V.; Gascon, J. *Langmuir* **2017,** 33, (50), 14278-14285.

18. Geng, D.; Yang, S.; Zhang, Y.; Yang, J.; Liu, J.; Li, R.; Sham, T.-K.; Sun, X.; Ye, S.; Knights, S. *Applied Surface Science* **2011,** 257, (21), 9193-9198.

19. Santa, M.; Posner, R.; Grundmeier, G. *J Electroanal Chem* **2010,** 643, (1), 94-101.

20. Chuang, T. J.; Brundle, C. R.; Rice, D. W. *Surface Science* **1976,** 59, (2), 413-429.

21. Thomas, L.; Arbouch, I.; Guerin, D.; Wallart, X.; Van Dyck, C.; Melin, T.; Cornil, J.; Vuillaume, D.; Lenfant, S. *Nanoscale* **2021,** 13, 6977-6990.

22. Engelkes, V. B.; Daniel Frisbie, C. *The Journal of Physical Chemistry B* **2006,** 110, (20), 10011-10020.

23. Smaali, K.; Desbief, S.; Foti, G.; Frederiksen, T.; Sanchez-Portal, D.; Arnau, A.; Nys, J. P.; Leclere, P.; Vuillaume, D.; Clement, N. *Nanoscale* **2015,** 7, (5), 1809-1819.

24. Cui, X. D.; Primak, A.; Zarate, X.; Tomfohr, J.; Sankey, O. F.; Moore, A. L.; Moore, T. A.; Gust, D.; Harris, G.; Lindsay, S. M. *Science* **2001,** 294, 571-574.

25. Cui, X. D.; Zarate, X.; Tomfohr, J.; Sankey, O. F.; Primak, A.; Moore, A. L.; Moore, T. A.; Gust, D.; Harris, G.; Lindsay, S. M. *Nanotechnology* **2002,** 13, 5-14.

26. Morita, T.; Lindsay, S. *J Am Chem Soc* **2007,** 129, (23), 7262-7263.

27. Johnson, K. L., *Contact Mechanics*. Cambridge University Press: New York, 1987.

28. WebElements, https://webelements.com.

29. Grüter, L.; Cheng, F.; Heikkilä, T. T.; González, M. T.; Diederich, F.; Schönenberger, C.; Calame, M. *Nanotechnology* **2005,** 16, (10), 2143-2148.

30. Brunner, J. Gaining Microscopic Insight into Molecular Junctions by Transport Experiments. Basel University, 2013.

31. Delmas, V.; Diez-Cabanes, V.; Van Dyck, C.; Scheer, E.; Costuas, K.; Cornil, J. *Physical Chemistry Chemical Physics* **2020,** 22, (46), 26702-26706.

32. Beebe, J. M.; Kim, B.; Gadzuk, J. W.; Frisbie, C. D.; Kushmerick, J. G. *PHYSICAL REVIEW LETTERS* **2006,** 97, (2), 026801.

33. Beebe, J. M.; Kim, B.; Frisbie, C. D.; Kushmerick, J. G. *ACS Nano* **2008,** 2, (5), 827-832.

34. Huisman, E. H.; Guédon, C. M.; van Wees, B. J.; van der Molen, S. J. *Nano Lett* **2009,** 9, (11), 3909-3913.

35. Mirjani, F.; Thijssen, J. M.; van der Molen, S. J. *Physical Review B* **2011,** 84, (11), 115402.

36. Bâldea, I. Physical Review B **2012,** 85, (3), 035442.

37. Ricoeur, G.; Lenfant, S.; Guerin, D.; Vuillaume, D. *Journal of Physical Chemistry C* **2012,** 116, (39), 20722-20730.

38. Bâldea, I. Physical Chemistry Chemical Physics **2015,** 17, (31), 20217-20230.

39. Büttiker, M.; Imry, Y.; Landauer, R.; Pinhas, S. *Physical Review B* **1985,** 31, (10), 6207-6215.

40. Heimel, G.; Rissner, F.; Zojer, E. *Adv. Mater.* **2010,** 22, (23), 2494-2513.

41. Crivillers, N.; Osella, S.; Van Dyck, C.; Lazzerini, G. M.; Cornil, D.; Liscio, A.; Di Stasio, F.; Mian, S.; Fenwick, O.; Reinders, F.; Neuburger, M.; Treossi, E.; Mayor, M.; Palermo, V.; Cacialli, F.; Cornil, J.; Samorì, P. *Adv. Mater.* **2013,** 25, (3), 432-436.

42. Rodriguez-Gonzalez, S.; Xie, Z.; Galangau, O.; Selvanathan, P.; Norel, L.; Van Dyck, C.; Costuas, K.; Frisbie, C. D.; Rigaut, S.; Cornil, J. *J. Phys. Chem. Lett.* **2018,** 9, (9), 2394-2403.